Journal of the Civil Engineering Forum, January 2024, 10(1):11-22
DOI 10.22146/jcef.7135
Available Online at https://jurnal.ugm.ac.id/v3/jcef/issue/archive

Parametric Study of the Effect of Diameter-to-Thickness Ratio Against Bending and Shear Load on the Behavior of Round Hollow Structural Section Beam

Mahmud Kori Effendi*, Hariadi Yulianto
Department of Civil Engineering, Universitas Islam Indonesia, Yogyakarta, INDONESIA
Jalan Kaliurang Km. 14,5 Yogyakarta
*Corresponding author: kori.effendi@uii.ac.id

SUBMITTED 04 March 2023 **REVISED** 06 June 2023 **ACCEPTED** 06 July 2023

ABSTRACT The steel-constructed buildings in Indonesia are on the rise, indicating a growing preference for their durability and versatility in construction projects. This led to the general application of Round Hollow Structural Section (Round HSS) as column and beam elements. Therefore, this study aimed to conduct parametric analysis of the effect of Diameter-to-Thickness Ratio ($D\ t^{-1}$) on the three-point and four-point flexural analysis of Round HSS beam using MSC Marc/Mentat software. Nonlinear materials and geometries were employed, along with the application of contact analysis, with contacted and contacting bodies. Moreover, the load and boundary condition were set to be similar to the experiment. The results showed that a greater $D\ t^{-1}$ led to the possibility of withholding a smaller load and causing smaller displacement in Group A with fixed diameter and different thickness values. Meanwhile, in Group B with fixed thickness but different diameters, a greater $D\ t^{-1}$ led to the potential of restraining more load and experiencing smaller displacement. All specimens from both groups were observed to have failed due to a combination of global and local buckling at the right location under the load applied. AISC bending moment calculated was found to be greater than the values obtained from the finite element analysis for all sections under three-point loads. It was also discovered in the four-point flexural analysis that the bending moment of noncompact section was greater than for AISC while those for the compact section were lower. Furthermore, shear strength (V_n) calculated was observed to be greater than shear force from finite element analysis ($P_{max}/2$).

KEYWORDS Round; Width-to-thickness Ratio; Three-loading Test; Four-loading Test; MSC MARC/MENTAT

1 INTRODUCTION

The main ingredients for affordable and readily available steel typically consist of iron and carbon. Using steel in construction offers benefits like faster building, cost efficiency, and quicker project completion. Steel with Round Hollow Structural Section (Round HSS) is observed to be generally used as both column and beam elements. An important function of beam elements in buildings is to carry the load distributed on the floor slab. However, Round HSS beam can potentially undergo local yielding, buckling, or failure before reaching its ultimate strength when subjected to excessive floor loads. According to the User Note Table F1.a in AISC 360, there are no specific requirements for flange and web slenderness for Round HSS, indicating empty information (AISC, 2022). Furthermore, in AISC 360, a steel section can be classified as compact, noncompact, or slender as shown in Figure 1a. A compact section typically develops a full plastic stress distribution and has a dimensionless rotational capacity (R) of about three before local buckling occurs. Meanwhile, A noncompact section can develop yield stresses in its compression elements before local buckling but cannot produce a rotational capacity, R, of three. On the other hand, a slender element profile is characterized by having sufficient slender plate components, which ensure the occurrence of local buckling within the elastic range. Chord rotation in calculating the R value can be seen in Figure 1b.

Round HSS was observed to have been widely used in several offshore pipe-building structures and deep-water platforms, as well as hotels, houses, and others. This was due to its structural behavior such as beam with width-to-thickness ratio ($D\ t^{-1}$) ranging between 16-48 and the very high tensile strength of steel between 450 to 1350 MPa as re-

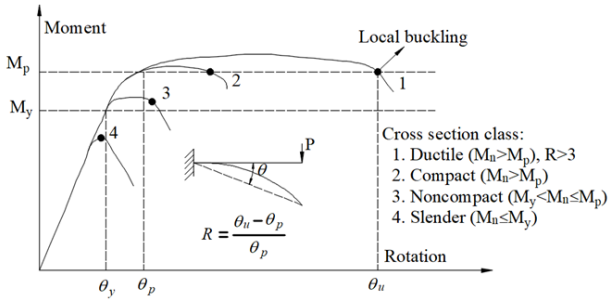

(a) The rotational capacity

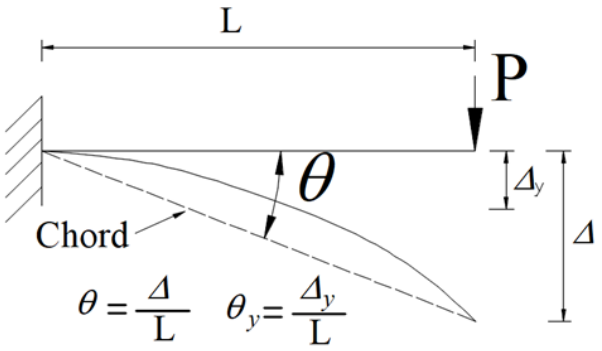

(b) Definition of chord rotation (rotation angle) (Niroomandi et al., 2015)

Figure 1 The chord rotation angle

ported in pure flexural and 4-point bending experiments. Moreover, the full plastic moment capacity of the section has been analyzed using up to 198 slenderness. Some studies also proposed a limit of 117 and 153 based on the R-value of 3 and 4, respectively (Jiao and Zhao, 2004). Chan and Gardner (2008) were observed to have tested 4- and 3-point flexures on elliptical hollow hot rolled steel beam while the flexural test data for Round HSS beam were used by Sherman (1986) and Gardner and Chan (2007) as a reference to analyze elliptical beam. Elchalakani et al. (2002) also tested 12 Round HSS beams with D t^{-1} ranging from 37 -122 and compared the findings with design regulations AS4100 (AS4100, 2020) while Guo et al. (2013) determined the effect of cross-sectional slenderness, D t^{-1}, from 75 to 300 on the inelastic and elastic flexural properties of thin-walled Round HSS beam. The influence of welded stiffeners on steel tube was also studied and the results showed an increase in beam capacity and specimen ductility. The experimental results were eventually compared with current design guidelines such as AISC-LRFD (AISC, 2005), AS4100 (AS4100, 2020), and Eurocode (BS, 2006).

AISC 360 (AISC, 2022): F8 applied to Round HSS required the width-to-thickness ratio for the element λ= D t^{-1}, to be less than 0.45E F_y without any specific mention of the minimum value limit. Moreover, the behavior and strength of Round HSS beam having λ= D t^{-1} higher than 0.45E F_y are not included in the article. This means there is a need to apply the finite element analysis to solve the related problems. Therefore, the method has been used in several studies to validate the experimental results of hollow beams. For example, Chan and Gardner (2008) used the finite element software, ABAQUS, to validate the experimental results of 3-point and 4-point hollow elliptical bending beam and Zhu et al. (2021) on elliptical hollow 4-point bending beam.

A study was conducted to investigate the impact of load shape tips including round, square, and diamond on compact beam subjected to midspan loads using MSC Marc/Mentat software (Effendi et al., 2014). Moreover, the finite element model from Effendi et al. (2015) was applied to parametric study of the D t^{-1} ratio against the strength of the flexural and shear of Round HSS beam. The 3D FEM model was developed with due consideration for the material and geometrical nonlinearities as well as the bearing action known to be influencing the accuracy of the results. The bearing action was also considered in the process of analyzing the contact between the loading plate and beam. Furthermore, Round HSS was modeled using 3D solid element type 7 (MSC, 2010) and the design flexural and shear strength were evaluated based on the Specifications for Structural Steel Buildings AISC 360 (AISC, 2022).

2 STRENGTH OF BEAM

2.1 Nominal Flexural Strength

AISC 360 classifies cross-sectional shapes as compact, non-compact, or slender, depending on the values of the width-to-thickness ratios under flexure in Section B4, “Member Properties,” (AISC, 2022) Table 1 summarized as follows.

1. If $\lambda \leqslant \lambda p$ and the flange is continuously connected to the web, the shape is compact

Table 1. Width-to-Thickness Ratios: Compression Elements Members Subject to Flexure (BSN, 2020)

Stiffened Elements	Description of Element	Width-to Thickness Ratio	Limiting Width-to-Thickness Ratio	
			λ_p (compact/noncompact)	λ_r (noncompact/slender)
	Round Hollow Structural Section	D/t	0.07 E/F_y	0.31 E/F_y

2. If $\lambda p < \lambda \leqslant \lambda r$, the shape is noncompact
3. If $\lambda > \lambda r$, the shape is slender.

Where λ refers as width-to-thickness ratio, λp as upper limit for the compact category, and λr as upper limit for noncompact category.

AISC 360, F8, applies to Round HSS with a width-to-thickness ratio, $\lambda = D\ t^{-1}$, less than $0.45E\ F_y^{-1}$. The nominal flexural strength, M_n, is required to be either the lowest value obtained according to the limit states of yielding (plastic moment) or local buckling as follows (AISC, 2022).

$$M_{n1} = M_p = F_y Z \tag{1}$$

Where Z is plastic section modulus (mm^3) and Fy is specified minimum yield stress (MPa).

Local Buckling

1. For sections with compact shapes, the limit state of local buckling for the flange does not apply.
2. For sections with noncompact shapes

$$M_{n2} = (\frac{0.021E}{D/t} + F_y)S \tag{2}$$

3. For sections with a slender shape

$$M_{n3} = F_{cr} S \tag{3}$$

where,

$$F_{cr} = \frac{0.33E}{D/t} \tag{4}$$

S refers to elastic section modulus about the axis of bending (mm^3), D as outside diameter of round HSS, in. (mm), and t as round hollow section thickness (mm).

The bearing action was assumed in this study to be the cause of local buckling and was developed based on the contact between the tip of the loading plate and beam.

2.2 Nominal Shear Strength

Nominal shear strength, V_n, of round hollow section was calculated according to the ultimate shear yield and shear buckling and was determined based on Article G5 of AISC 360 (AISC, 2022) as follows:

$$V_n = \frac{F_{cr} A_g}{2} \tag{5}$$

where: F_{cr} was required to be the greatest value between

$$F_{cr1} = \frac{1.6E}{\sqrt{\frac{L_v}{D}}[\frac{D}{t}]^{5.4^{-1}}} \tag{6}$$

and

$$F_{cr2} = \frac{0.78E}{[\frac{D}{t}]^{3.2^{-1}}} \tag{7}$$

but not more than the value of $0.6F_y$.

Where A_g is gross cross-sectional area of structural members (mm^2), D is outer diameter (mm), L_v is distance from the location of the maximum shear force to the zero shear force (mm), and t is thickness of wall design (mm).

Shear buckling equations, Equation 6 and Equation 7, are normally used for the $D\ t^{-1}$ was above 100, high-strength steel, and beam long span. Meanwhile, the shear yielding applied for standard profiles and $F_{cr} = 0.6F_y$.

3 LOCAL BUCKLING LIMIT STATE

The main internal actions on beam subjected to a transverse load are usually on its cross-section in the form of the bending moment, M, and shear force, V. The equations to be used in the design are normally governed by the section classification. For example, the compact section is capable of attaining full plastic moments before experiencing local buckling effect. This simply means the local buckling effect can be completely ignored

Table 2. Local Buckling Limit State-Flexural Strength Relationship (Mahamid et al., 2020)

Classification of the compression element	Limiting Width-to-Thickness Ratio	Failure mode	Nominal flexural capacity
Compact	$\lambda \leqslant \lambda_p$	Plastic hinge formation	$M_{n1} = M_p$
Noncompact	$\lambda_p < \lambda \leqslant \lambda_r$	Inelastic local buckling	$M_y < M_{n2} < M_p$
Slender	$\lambda_r < \lambda$	Elastic local buckling	$M_{n3} < M_y$

in the design. Meanwhile, local buckling is experienced in the noncompact section before the development of the full plastic moment and after the onset of the first yield. For the slender section, local buckling is expected to occur before the first yield of material due to bending. Therefore, the equations for local buckling limits and beam flexural capacities of each section classification are summarized in the following Table 2 (Mahamid, 2020).

Where M_y is the yield moment about the axis of bending (Nmm):

$$M_y = F_y S \tag{8}$$

4 PLASTIC LOAD

The information presented in SIA 265 (SIA265, 2012) shows that two lines are used in the load-displacement curve to determine plastic load (Ppl). The first line represents initial stiffness (K_α), which is usually calculated from 10% to 40% of the maximum load, and forms an angle α with the displacement axis. Meanwhile, second line (K_β), is drawn at a slope equal to one-sixth of the secant line slope in the load-displacement curve. Plastic load is determined as the intersection of those two lines (K_α and K_β) as presented in Figure 2.

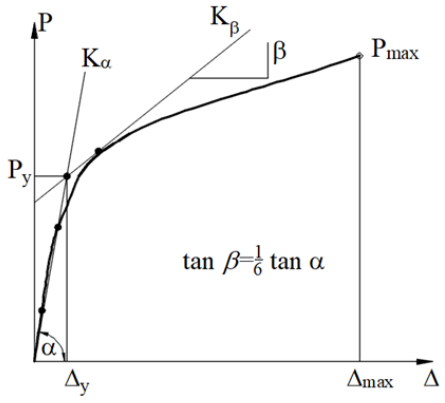

Figure 2 Definition of plastic strength

5 STUDY METHODOLOGY

5.1 Finite Element Modeling

Finite element modeling is one of the optimal ways to reproduce the experimental response of tubular steel beam structures. It was conducted in this study using the commercial finite element software MSC Marc/Mentat (MSC, 2003) through both nonlinear material and geometrical approaches. The process required making an exact model of the laboratory specimen in terms of dimensions, boundary conditions, and loading system. The loading elements were modeled using surface geometry while steel tube was based on the solid elements (Type 7 MSC Marc/Mentat). Moreover, Figure 3 shows that the mesh size of the solid element under the load surface was 8.3x16x3.2 and this was smaller compared to those far from the load with 16.6x16.6x3.2. It was also observed that a shell element (Type 75 MSC Marc/Mentat) (MSC, 2010) was used for the end support.

The mechanical properties of steel tube used in this study are presented in the following Table 2. It was discovered that beam specimen was in the range of λ= (D t^{-1}) less than 0.45(E F_y^{-1}) = 0.45 (211000/386) = 245. Steel parts were modeled in FE analysis as bilinear elastic plastic material, the yield stress (F_y) and tensile stress of tube were recorded to be 386 MPa and 520 MPa, respectively, while the modulus of elasticity (E) was 211 GPa and Poisson's ratio (v) was 0.3. Steel plate was an elastic material and the boundary conditions of the support were observed to be pin-roller supports but the loading was simulated to determine the conditions to be used during the experiment as presented in Figure 4. Moreover, the displacement loading was controlled by setting the loading geometry to move downward by 120 mm. It was also observed that beam span was 996 mm.

The downward movement of the rigid geometry for

Table 3. Mechanical Properties of Parametric Study

	Section	D (mm)	t (mm)	λ=D t^{-1}	λ_p	λ_r	Beam Classification	Ag (mm^2)	Z (cm^3)	S (cm^3)
Group A	CVSt12	114.3	1.2	95.2	38.2	169.4	Noncompact	426.3	15.4	11.9
	CVSt22	114.3	2.2	51.9	38.2	169.4	Noncompact	774.7	27.6	21.3
	CVSt32*	114.3	3.2	35.7	38.2	169.4	Compact	1116.8	39.5	30.1
	CVSt42	114.3	4.2	27.2	38.2	169.4	Compact	1452.7	50.9	38.5
	CVSt52	114.3	5.2	21.9	38.2	169.4	Compact	1782.2	61.9	46.5
	CVSt62	114.3	6.2	18.4	38.2	169.4	Compact	2105.5	72.5	53.9
Group B	CVSd250	250.0	3.2	78.1	38.2	169.4	Noncompact	2481.1	194.9	151.1
	CVSd200	200.0	3.2	62.5	38.2	169.4	Noncompact	1978.4	123.9	95.8
	CVSd150	150.0	3.2	46.8	38.2	169.4	Noncompact	1475.7	68.9	53.0
	CVSd100	100.0	3.2	31.2	38.2	169.4	Compact	973.1	29.9	22.8
	CVSd75	75.0	3.2	23.4	38.2	169.4	Compact	721.8	16,5	12.4
	CVSd50	50.0	3.2	15.6	38.2	169.4	Compact	470.4	7.0	5.2

* reference (Effendi et al., 2015),

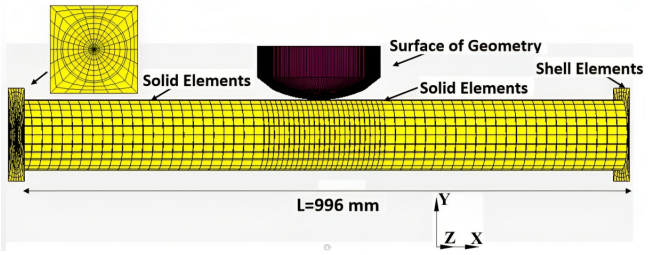

Figure 3 The mesh of FEM model

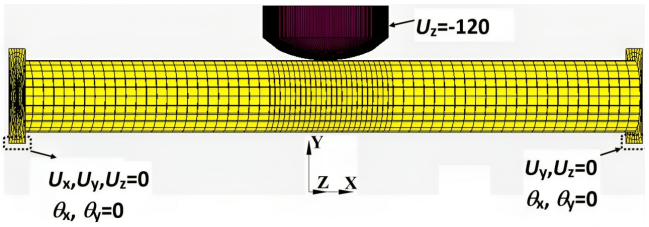

Figure 4 The loading plate, boundary, and support conditions

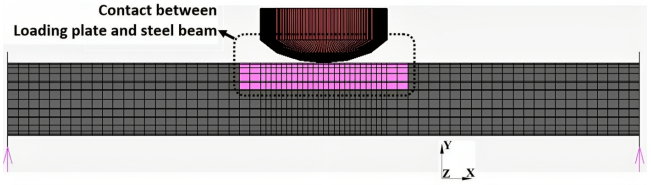

Figure 5 Contact analysis

the loading surface was used to provide contact as shown in Figure 5. Furthermore, the contact between the surfaces of the loading plate and steel tube was used to model the loading as a touching contact type without friction. This allowed the possibility of separation without any form of penetration between the contacting and contacted bodies.

6 RESULTS AND DISCUSSION

6.1 Load-Displacement Response and Failure Modes of Specimen Reference

The finite element analysis was compared to the experimental load-midspan displacement curves derived for the steel tubular beam by Effendi et al. (2015) as presented in Figure 6. It was discovered that the curve was generally characterized by both elastic and inelastic range. The load-displacement behaviour was also determined based on the distinct patterns on the curve and the linear curve observed during the elastic phase shifted to a quadratic curve during the inelastic phase. Subsequently, there was a gradual decrease in load as the displacement angle increased after reaching the peak load. It was also found that the finite element analysis did not precisely replicate the experimental results as shown by the slight disparity between the two curves but they both generally had a consistent trend. The finite element analysis curve was wavy due to the complexities of the contact model between the loading plate and beam, along with the need for a more stringent convergence tolerance value. The results effectively showed that the finite element model developed for steel tube beam effectively captured the load-displacement response observed in the experimental test.

The final failure shape of round steel tube beam presented in Figure 7 showed that beam generally experienced a form of global flexural failure along with local buckling failure just below the loading plate. Moreover, the shape of local buckling re-

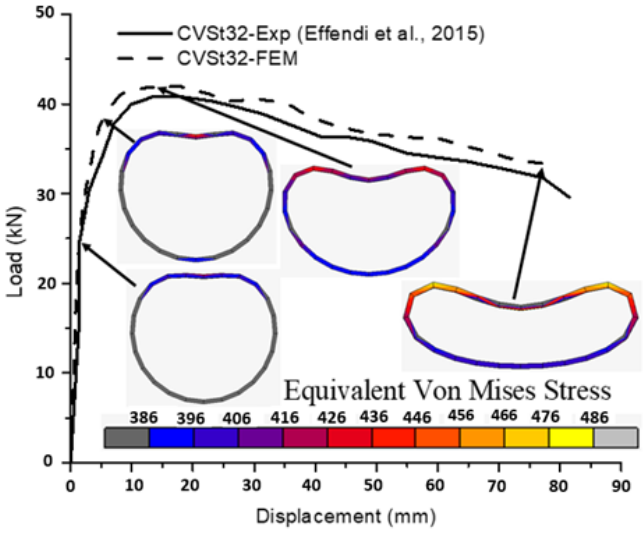

Figure 6 Load–displacement response

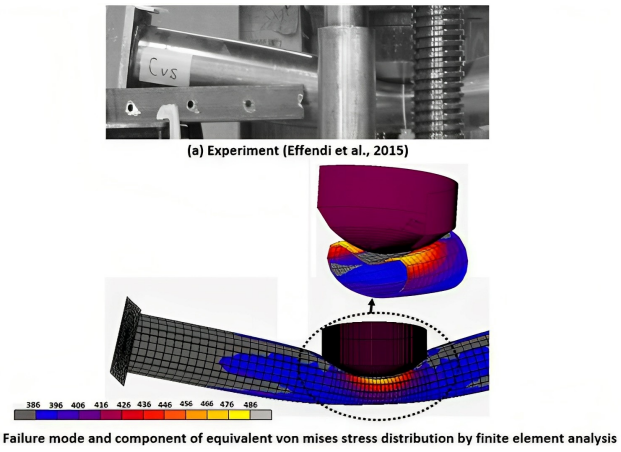

Figure 7 Failure of beam

sembled the loading plate tip as presented in Figure 7b and the results of the finite element modeling were observed to be similar to those obtained from the experiment. Local buckling was also found below the loading plate element while the yield stress concentration was identified under the loading plate placed on the top sides of the steel beam. This yield stress concentration affected the load-carrying capacity of the specimen as shown in the descending part of the load-displacement curve in Figure 6. Furthermore, the capacity of steel beam could be governed by buckling failure before full plastic resistance was developed during the subjection of the elements to compressive stresses (Kamruzzaman et al., 2017). This phenomenon was presented in Figure 7b where the compressive stress of component 1-1 was not fully plastic because of local buckling failure.

6.2 Load-Displacement Response from Parametric Study of D t^{-1}

Three- and four-point bending tests are commonly used to determine the flexural strength of specimen. It was observed that the finite element modeling applied produced appropriate results compared to the experiment and this led to the subsequent usage of the model to conduct parametric studies. This was achieved by dividing the data into two groups including Group A where the value of the diameter was fixed and the thickness varied and Group B where the value of the thickness was fixed and the diameter varied. All beams were loaded with a displacement control of 120 mm which was exactly the same as the reference beam loading value. Figure 8a shows the load-displacement curve for Group A with the displacement measured below the middle of beam span. The results showed that the CVSt12 beam (D t^{-1} =92.25) had the smallest maximum load of 11.1 kN while the CVSt62 beam (D t^{-1} = 18.44) had the largest with 105 kN. The CVSt12 beam (D t^{-1} = 92.25) also had the lowest maximum displacement of 55.8 mm while the CVSt62 beam (D t^{-1} = 18.44) had the highest with 99.5 mm. Furthermore, the results of the three-point flexural analysis were compared with those of the four-point where two loads were placed at a distance L/3 from the supports. Figure 8b shows that the CVSt12 beam (D t^{-1} = 92.25) had the smallest peak load of 17.9 kN and the CVSt62 beam (D t^{-1} = 8.44) had the largest with 161 kN. The CVSt12 beam (D t^{-1} = 92.25) also had the lowest displacement value of 72 mm while the CVSt62 beam (D t^{-1} = 18.44) had the highest with 126 mm. The results further showed that beam with the D t^{-1} range from 18.44 to 92.25 experienced a linear decrease in the load after reaching the peak, showing the possibility of restraining smaller loads at higher D t^{-1} in Group A. The thickness of steel tube beam was also found to be affecting the load value to be restrained and this was shown by the fact that a higher D t^{-1} led to smaller displacement in Group A.

The results of the three-point flexural analysis presented in Figure 9a showed that the CVSd50 beam (D t^{-1} = 15.63) had the smallest load of 11.5 kN in Group B and the CVSd250 beam (D t^{-1} = 78.13) had the largest with 137 kN. The displacement on the lower side of the center span for the CVSd50 beam (D t^{-1} = 15.63) was the largest with

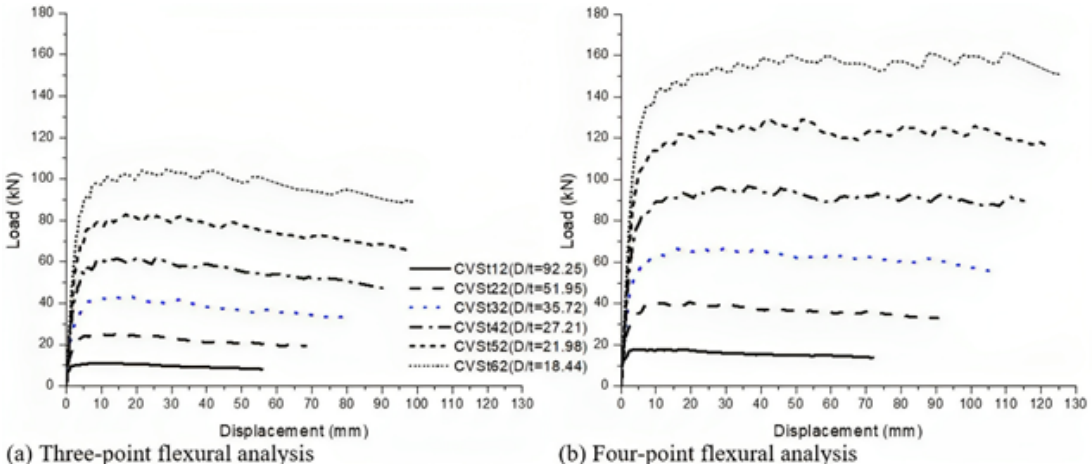

Figure 8 Load–displacement response for Group A

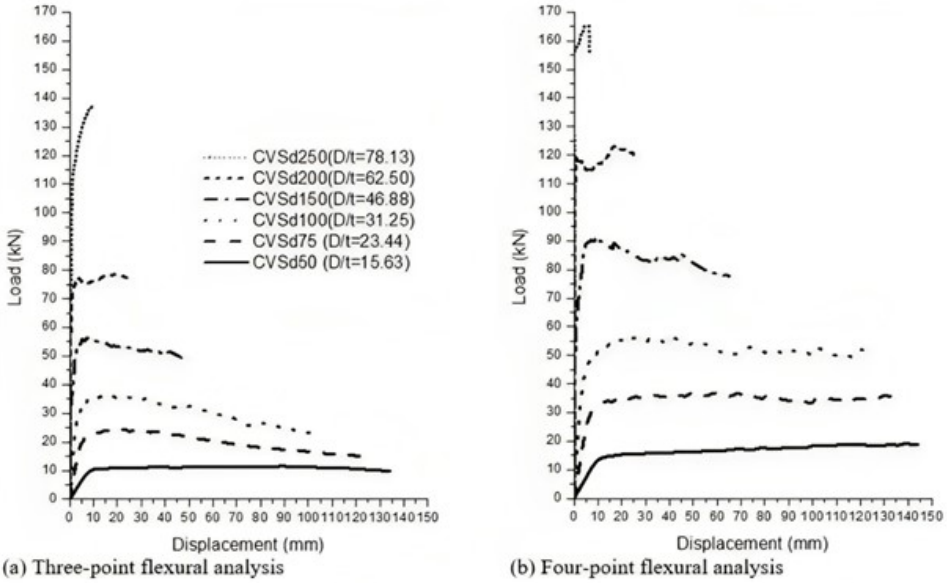

Figure 9 Load–displacement response for Group B

134 mm while the CVSd250 beam (D t^{-1} = 78.13) had the smallest at 9.22 mm. The results of the four-point flexural analysis presented in Fig. 9(b) also showed that the CVSd50 beam (D t^{-1} = 15.63) had the smallest load of 19.1 kN and the CVSd250 beam (D t^{-1} = 78.13) had the greatest with 165 kN. The displacement on the lower side of the center span for the CVSd50 beam (D t^{-1} = 15.63) was the largest with 144 mm while the CVSd250 beam (D t^{-1} = 78.13) had the smallest at 6.43 mm. The trend showed that a higher D t^{-1} led to the possibility of restraining more loads in Group B and this was different from the observations made in Group A. Meanwhile, a higher D t^{-1} was discovered to have led to smaller displacement which was similar to the phenomenon in Group A.

6.3 Failure Mode from Parametric Study of D t^{-1}

The nonlinear finite element analysis previously explained in Chapter 6.1 was observed to have the capacity to capture the failure mode of experimental results. The observation from the three-point flexural analysis of Group A summarized in Figure 10 showed that beam with D t^{-1} between 35.75 (CVSt32) and 95.25 (CVSt12) had a flat oval failure on the upper side while those between 18.44 (CVSt62) and 27.21 (CVSt42) had a concave oval shape. A similar trend was identified for Group B in Figure 11 where D t^{-1} between 46.88 (CVSd150) and 78.13 (CVSd250) was observed to have a flat oval failure on the top side while those between 15.63 (CVSd50) and 31.25 (CVSd100) had a concave oval shape. Moreover, all the specimens from

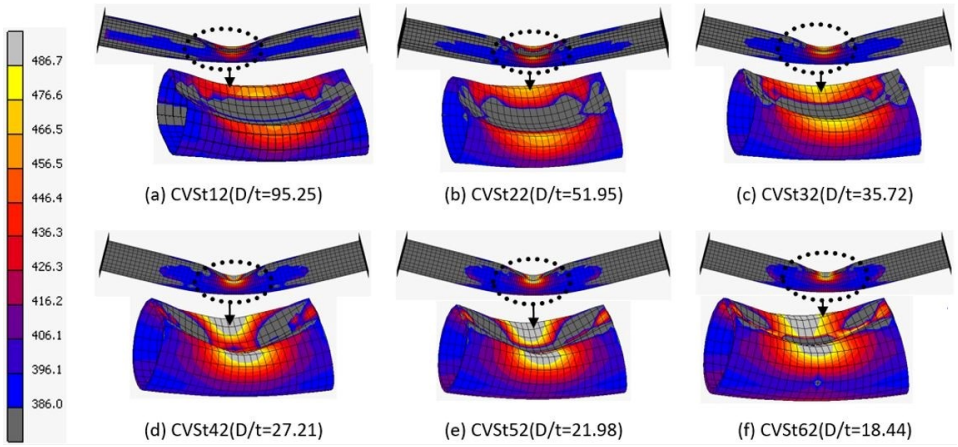

Figure 10 Failure mode and equivalent von mises stress of Group A in three-point flexural analysis

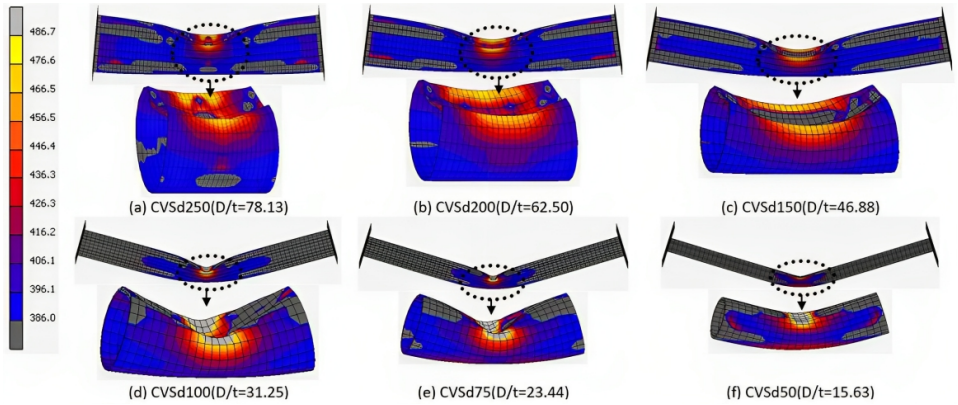

Figure 11 Failure mode and equivalent von mises stress of Group B in three-point flexural analysis

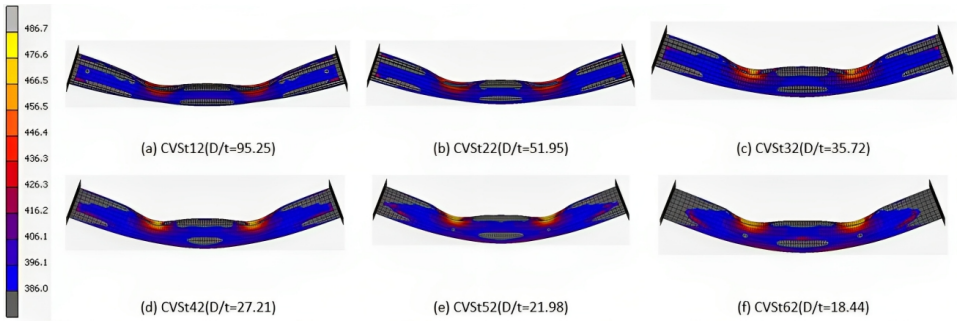

Figure 12 Failure mode and equivalent von mises stress of Group A in four-point flexural analysis

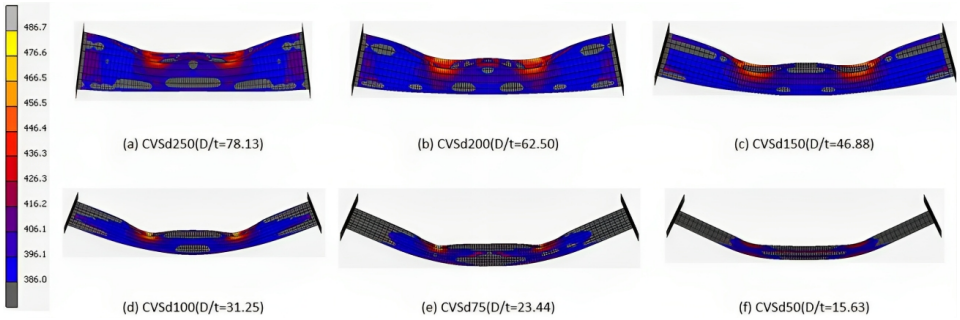

Figure 13 Failure mode and equivalent von mises stress of Group B in four-point flexural analysis

Table 4. Summary of parametric study using three-point flexural analysis

Group	Section	D t^{-1}	Mn (kNm)		FEM		Mn/Mpl	Mn/M_{max}	R	V_n (kN)	$P_{max}/2$ (kN)	V_n / $P_{max}/2$
			M_{n1}	M_{n2}	Mpl	M_{max}						
A	CVSt12	95.2		5.1	2.5	2.8	2.2	1.9	9.5	37.7	5.55	6.8
	CVSt22	51.9		10.1	5.7	6.2	1.8	1.7	7.9	89.7	12.6	7.1
	CVSt32*	35.7	15.2		9.4	10.6	1.7	1.5	8.2	129.3	21.4	6.0
	CVSt42	27.2	19.6		14.1	15.3	1.5	1.4	8.3	168.2	30.8	5.5
	CVSt52	21.9	23.9		18.6	20.6	1.4	1.2	8.4	206.4	41.4	5.0
	CVSt62	18.4	27.9		24.4	26.1	1.2	1.1	8.7	243.8	52.5	4.6
B	CVSd250	78.1		66.9	28	34.1	2.5	2.1	7.4	287.3	5.75	50.0
	CVSd200	62.5		43.7	17.7	19.5	2.6	2.4	11.7	229.1	12.2	18.8
	CVSd150	46.8		25.4	12.7	14.0	2.1	1.9	10.9	170.9	18.1	9.4
	CVSd100	31.2	11.5		8.2	9.0	1.5	1.4	12.2	112.7	28.2	4.0
	CVSd75	23.4	6.3		5.7	6.1	1.2	1.1	10.4	83.6	39.2	2.1
	CVSd50	15.6	2.7		2.7	2.8	1	1	11.5	54.5	68.5	0.8

both groups failed due to a combination of global and local buckling at the exact location under the load applied. For Group A, the width of equivalent von mises stress that was greater than the yield stress of CVSt12 (D t^{-1} = 95.25) beam was higher compared to CVSt62 (D t^{-1} = 18.44) as presented in Figure 10. This showed that beam with smaller thickness CVSt12 (D t^{-1} = 95.25) restrained smaller load compared to those with higher thickness CVSt62 (D t^{-1} = 18.44). For Group B, the width of equivalent von mises stress that was greater than the yield stress of CVSd50 (D t^{-1} = 15.63) beam was observed to be smaller compared to CVSd250 (D t^{-1} = 8.13). This showed beam with a smaller diameter CVSd50 (D t^{-1} = 15.63) was able to restrain a smaller load compared to those having a higher diameter CVSd250 (D t^{-1} = 78.13). Meanwhile, all beams in both groups experienced a full plastic section under load due to stress concentrations in local buckling area. It was also discovered that only CVSd250 (D t^{-1} = 78.13), CVSd200 (D t^{-1} = 62.50), and CVSd150 (D t^{-1} = 46.88) identified as noncompact beam had yield stress close to both supports.

The failure mode obtained through four-point flexural analysis for beam in Groups A and B is presented in Figures 12 and 13, respectively. It was discovered that local buckling was not as deep as those reported in the three-point analysis, making it possible for beam to support more loads. For Group A, the equivalent von mises stress was found to be greater than yield stress concentration under load and near the middle of the span for CVSt52 (D t^{-1} = 1.98) and CVSt62 (D t^{-1} = 8.44) but only under load for CVSt12 (D t^{-1} = 95.25), CVSt22 (D t^{-1} = 51.95), CVSt32 (D t^{-1} = 35.72), and CVSt42 (D t^{-1} = 27.21) as shown in Figure 12. For Group B, the equivalent von mises stress was also identified to be greater than yield stress under the load and near the mid-span for CVSd100 (D t^{-1} = 31.25), CVSd75 (D t^{-1} = 23.44), and CVSd50 (D t^{-1} = 15.63) but under the load and near the supports for CVSd250 (D t^{-1} = 78.13), CVSd200 (D t^{-1} = 62.50), and CVSd150 (D t^{-1} = 46.88) noncompact beam as presented in Figure 13.

6.4 Flexural and Strength Comparison with available Steel Specifications

Some specifications are available to design the flexural and shear strength of round hollow steel tube such as the American AISC LRFD (AISC360, 2016), Australian AS4100 (AS4100, 2020), and European Specification (BS, 2006). The Indonesian Steel specification was also adopted from AISC LRFD (BSN, 2020). The results obtained from the finite element analysis and applied in parametric studies were compared to the analytical calculation according to Specifications for Structural Steel Buildings AISC 360 (AISC, 2022) for verification purposes.

The yielding moment (M_{n1}) was calculated using Equation 1, local buckling moment (M_{n2}) through Equation 2 for noncompact section, and beam shear strength, V_n, using Equation 5. The compact sections (CVSt32, CVSt42, CVSt52, CVSt62, CVSd100, CVSd75, and CVSd50) were evaluated using Equation 1 while the noncompact sections (CVSt12, CVSt22, CVSd250, CVSd200, and

Table 5. Summary of parametric study using four-point flexural analysis

Group	Section	D t^{-1}	Mn (kNm)		FEM		M_n/Mpl	M_n/M_{max}	R	V_n (kN)	$P_{max}/2$ (kN)	V_n / $P_{max}/2$
			M_{n1}	M_{n2}	Mpl	M_{max}						
A	CVSt12	95.2		5.1	4.2	4.4	1.2	1.2	15.4	37.7	8.9	4.2
	CVSt22	51.9		10.1	9.4	9.9	1.1	1.0	8.6	89.7	20.3	4.4
	CVSt32*	35.7	15.2		15.6	16.4	1.0	0.9	7.9	129.3	33.3	3.9
	CVSt42	27.2	19.6		22.6	23.1	0.9	0.8	8.7	168.2	48.4	3.5
	CVSt52	21.9	23.9		29.6	32.1	0.8	0.7	9.0	206.4	64.5	3.2
	CVSt62	18.4	27.9		37.5	40.1	0.7	0.7	9.1	243.8	80.5	3.0
B	CVSd250	78.1		66.9	38.9	41.3	1.7	1.6	3.0	287.3	82.9	3.5
	CVSd200	62.5		43.7	30.1	30.8	1.5	1.4	9.7	229.1	61.8	3.7
	CVSd150	46.8		25.4	22.1	22.6	1.1	1.1	12.1	170.9	45.5	3.8
	CVSd100	31.2	11.5		13.6	14.2	0.8	0.8	10.1	112.7	28.5	4.0
	CVSd75	23.4	6.3		8.9	9.3	0.7	0.7	9.6	83.6	18.8	4.4
	CVSd50	15.6	2.7		4.2	5.0	0.6	0.5	12.8	54.5	10.1	5.4

CVSd150) were through Equation 2. The Ppl value was also determined from Chapter 4, the Mpl was calculated using the principle of moment, the P_{max} value was obtained from the maximum value of the load-displacement response produced using finite element analysis, and the M_{max} was estimated using the principle of moment. The summaries of parametric studies conducted using three- and four-point flexural analysis are presented in Tables 4 and 5 respectively. The results in Table 4 showed that the three-point flexural moment of Group A and Group B was greater than those obtained from the finite element analysis. All beams in both groups were observed to have overestimated moment capacity of the section due to local buckling.

The results in Table 5 showed that the four-point flexural moment of the non-compact sections of Group A (CVSt12, CVSt22) and Group B (CVSd250, CVSd200, CVSd150 was greater than those from the finite element analysis. The overestimation was also found to be due to local buckling. However, the results for the compact section of Group A (CVSt12, CVSt22) and Group B (CVSd250, CVSd200, CVSd150) were found to be lower than the finite element analysis. The calculated shear strength (V_n) was also higher than the shear force from the finite element analysis ($P_{max}/2$).

7 CONCLUSION

In conclusion, three-point finite element analysis conducted using MSC Marc/Mentat software was able to capture the experimental result effectively in terms of load-displacement response and failure mode shape. Parametric study showed that a higher D t^{-1} led to the restrain of smaller load and displacement in Group A consisting of beam with fixed diameter and varied thickness. It was discovered that the thickness of steel tube beam affected the load to be restrained. Meanwhile, a higher D t^{-1} led to the restraining of more loads and also caused smaller displacement in Group B consisting of beam with fixed thickness and varied diameter. The results further showed that all specimens from both groups failed in three-point and four-point flexural analysis due to the combination of global and local buckling at an exact location under the load applied. Furthermore, the flexural moment calculated using AISC for compact and noncompact sections under three-point load was found to be higher than those from the finite element analysis. The flexural moment of noncompact section from the four-point flexural analysis was discovered to be greater than those calculated using AISC but the values for the compact section were lower. The results also showed that the calculated shear strength (V_n) was higher than the shear force produced from the finite element analysis ($P_{max}/2$).

DISCLAIMER

The authors declare no conflict of interest.

ACKNOWLEDGMENTS

The authors are grateful to Jurusan Teknik Sipil, Universitas Islam Indonesia, for providing the

funds as well as Hariadi Yulianto, S.T., M.Eng. and Habib Abdurrahman for the assistance in this study.

REFERENCES

AISC (2022), *ANSI/AISC 360-22, Specification for Structural Steel Buildings*, Chicago AISC.

AISC, A. I. o. S. C. (2005), *Steel Construction Manual*.

AISC360, A. I. o. S. C. (2016), *Specification for Structural Steel Buildings*.

AS4100, S. A. (2020), *Steel Structures*.

BS (2006), Eurocode 3—design of steel structures—, Technical report, BS EN 1993-1, 1, p.2005.

BSN, B. S. N. (2020), *SNI 1729: 2020 Spesifikasi Untuk Bangunan Gedung Baja Struktural*, Jakarta.

Chan, T. and Gardner, L. (2008), 'Bending strength of hot-rolled elliptical hollow sections', *Journal of Constructional Steel Research* **64**(9), 971–986.

Effendi, M., Kawaguchi, H., Minami, K. and Kawano, A. (2015), 'An analytical study on effect of loading tip shapes on flexural behavior of vacant and concrete-filled steel tubular members subjected to concentrated transverse loads', *Kou kouzou rombunshuu* **22**(86), $86_33 - -86_45$.

Effendi, M., Zaitsu, S., Kawaguchi, H., Kawano, A., Matsuo, S., Tsuda, K. and Kido, M. (2014), 'Finite element analysis of vacant tubular members under static loading considering the tip shapes of load', *Applied Mechanics and Materials* .

Elchalakani, M., Zhao, X. and Grzebieta, R. (2002), 'Bending tests to determine slenderness limits for cold-formed circular hollow sections', *Journal of Constructional Steel Research* **58**(11), 1407–1430.

Gardner, L. and Chan, T. (2007), 'Cross-section classification of elliptical hollow sections', *Steel and Composite Structures* **7**(3), 185.

Guo, L., Yang, S. and Jiao, H. (2013), 'Behavior of thin-walled circular hollow section tubes subjected to bending', *Thin-Walled Structures* **73**, 281–289.

Jiao, H. and Zhao, X.-L. (2004), 'Section slenderness limits of very high strength circular steel tubes in bending', *Thin-Walled Structures* **42**(9), 1257–1271.

Kamruzzaman, M., Jumaat, M., Sulong, N., Qeshta, I. and Narmashiri, K. (2017), Effects of lateral bracing and stiffeners on the cfrp failure of strengthened steel beams, *in* 'IOP Conference Series: Materials Science and Engineering', IOP Publishing, p. 12021.

Mahamid, M. (2020), *Design Of Steel And Composite Members. Structural Engineering Handbook, Fifth Edition*.

MSC (2003), *MSC Software corporation*, Santa Ana, CA.

MSC, . S. C. (2010), *Volume B: Element Library*.

Niroomandi, A., Pampanin, S., Dhakal, R. and Soleymani Ashtiani, M. (2015), Comparison of alternative assessment procedures to predict seismic performance of rc columns, *in* 'Proceedings of tenth Pacific conference on earthquake engineering', Sydney, Australia.

Sherman, D. (1986), Inelastic flexural buckling of cylinders, *in* M. Pavlovic, ed., 'Steel Structures: Recent Research Advances and Their Applications to Design', Elsevier Applied Science Publishers, p. 339–357.

SIA265, S. S. A. (2012), *Timber structures*.

Zhu, J.-H., Su, M.-N., Zhu, X., Daniels, J. and Young, B. (2021), 'Flexural behaviour of cold-formed steel oval hollow section beams', *Journal of Constructional Steel Research* **180**, 106605.

[This page is intentionally left blank]